CHARACTERIZING LANDSLIDE MOVEMENT AT THE BOULDER CREEK

EARTHFLOW, NORTHERN CALIFORNIA, USING L-BAND INSAR

by

LAURA LYN STIMELY

A THESIS

Presented to the Department of Geological Sciences
and the Graduate School of the University of Oregon
in partial fulfillment of the requirements
for the degree of
Master of Science

September 2009

"Characterizing Landslide Movement at the Boulder Creek Earthflow, Northern

California, Using L-band InSAR," a thesis prepared by Laura Lyn Stimely in partial

fulfillment of the requirements for the Master of Science degree in the Department of

Geological Sciences. This thesis has been approved and accepted by:

_____

Joshua J. Roering, Chair of the Examining Committee

_____

___31-August-2009___

Date

Committee in Charge: Dr. Joshua J. Roering, Chair
                              Dr. David A. Schmidt
                              Dr. John M. Logan

Accepted by:

_____

Dean of the Graduate School

An Abstract of the Thesis of

Laura Lyn Stimely   for the degree of   Master of Science

in the Department of Geological Sciences   to be taken   September 2009

Title: CHARACTERIZING LANDSLIDE MOVEMENT AT THE BOULDER CREEK

EARTHFLOW, NORTHERN CALIFORNIA, USING L-BAND INSAR

Approved: _____

Joshua J. Roering

Spatial and temporal patterns of movement of the Boulder Creek earthflow were investigated using 26 interferograms derived from ALOS satellite radar images acquired between February 2007 and February 2008. Persistently unstable hillslopes in Northern California are ideally suited to the study of the dynamics and morphological signature of earthflows, as the deeply sheared mélange lithology, high seasonal rainfall, and fast uplift rates promote widespread deep-seated landsliding. In addition to identifying multiple active landslides in the region, L-band InSAR reveals varying deformation rates in the accumulation, transport, and toe regions of the Boulder Creek earthflow. Downslope displacement rates up to 1.8 m/yr are observed on the earthflow over a 1-year period. The pattern of deformation is similar to that observed from 1944-2006 inferred from aerial photography. Interferograms highlight spatially variable rates controlled by lithology and gullies, and movement correlates with seasonal rainfall with a phase lag of ~2 months.

CURRICULUM VITAE

NAME OF AUTHOR: Laura Lyn Stimely

PLACE OF BIRTH: State College, Pennsylvania, USA

DATE OF BIRTH: June 4, 1982

GRADUATE AND UNDERGRADUATE SCHOOLS ATTENDED:

>   University of Oregon, Eugene, OR
>   The Pennsylvania State University, University Park, PA

DEGREES AWARDED:

>   Master of Science, Geology, 2009, University of Oregon
>   Bachelor of Science, Engineering Science & Mechanics, 2005, The Pennsylvania
>   State University

AREAS OF SPECIAL INTEREST:

>   Geomorphology
>   Satellite Interferometry

PROFESSIONAL EXPERIENCE:

>   Graduate Teaching Fellow, Department of Geological Sciences, University of
>   Oregon, Eugene, OR, 2007-2009
>
>   Engineer, Bettis Atomic Power Laboratory, West Mifflin, PA, 2005-2007
>
>   Engineering Intern, Data Storage Institute, Singapore, 1/2005-7/2005
>
>   Technical Documentation Writer & Assistant, Minitab, Inc., State College, PA,
>   2000-2005
>
>   Geochemistry Laboratory Assistant, Materials Characterization Laboratory, Penn
>   State University, 2000-2001

PUBLICATIONS:

Roering J, Stimely L, Schmidt D, Mackey B (2009). Landslide movement and sediment production quantified with InSAR, airborne LiDAR, and archival air photos. Submitted to Geophysical Research Letters.

ACKNOWLEDGMENTS

I give my most sincere thanks to Professors Josh Roering and David Schmidt for their valuable support in the prepration of this manuscript and for their generosity and insight throughout the research process. Josh and David have provided me a positive environment to mature as a scientist, I am forever indebted to them for the skills I have learned and the patience they have shown. I especially want to thank my third thesis committee member John Logan for his honesty and kindness. I also would like to thank my family and friends for all of their support both academically and emotionally.

TABLE OF CONTENTS

LIST OF FIGURES

CHAPTER I

INTRODUCTION

Landslides frequently occur in hilly and mountainous areas, both presenting a

significant natural hazard and having profound effects on the landscape. Hillslopes adjust

their shape via diffusion creep and mass wasting in response to external forces such as

uplift, weathering, and climate change (e.g. Cruden and Varnes, 1996). Over geologic

timescales slope angles adjust to incision and uplift rates. Uplift usually results in

increased fluvial incision, which lowers base level and increases slope angles (Burbank

and Anderson, 2001). Hillslopes adjust to oversteepening via mass wasting processes,

which quickly removes material and reduces slope angles. Hillslopes have been observed

to maintain slope angles up to a particular threshold. *Burbank et al.* (1996) argued for

such a balance between uplift and erosion in the Himalayas where landsliding appears to

prevent slopes from continuing to steepen as uplift and incision increase. The idea can be

likened to a pile of sand, which can maintain slopes no steeper than its angle of repose.

Oversteepening, by adding material near the top of the pile or removing material near the

bottom, inevitably results in a landslide of material and relatively constant slopes.

Landslide activity also varies on short timescales. Seasonal precipitation has been shown

to play a large role in the activity of landslides (e.g. Keefer and Johnson, 1983; Iverson

and Major, 1987). Increased displacements have been observed during El Niño years and winter storms have resulted in earthflow surges of up to tens of meters in a day (Calabro, 2008; Iverson & Major, 1987). By studying landslides over broad areas and timescales, we seek to decipher the signature of past and present landslides on the landscape and what forces drive these features.

Detecting and monitoring landslide behavior tends to be highly site-specific and costly (Iverson & Major, 1987; Kelsey, 1978). Techniques such as leveling and GPS reveal valuable information about earthflow movement but may not be suitable to reveal detailed spatial heterogeneities and can only be maintained for a relatively limited period of time. Regional studies tend to be coarse, using data such as aerial photographs or digital elevation models to identify locations and timing of landslides (Hovius et al., 1997; Hovius et al., 2000; Fuller et al., 2004). Quantifying the spatial and temporal patterns of movement at high spatial resolution and over a broad area will provide insight into what a landslide-dominated landscape can tell us about the interplay between hillslope evolution and tectonic and climate processes at work.

Earthflows are among the most common mass-movement phenomena in nature. They are identified by round scarps, inflated toes, and by long narrow teardrop-shaped forms. Earthflows commonly display evidence of both fluid-like flow and rigid body translation. They occur in weak, fine-grained sediments. Earthflows often extend from ridge to channel and are typically found on relatively uniform slopes (Keefer and Johnson, 1983). The continuous and slow-moving nature of earthflows offers an excellent laboratory in which to study their short and long-term behavior and triggers.

The primary data for this study is L-band Interferometric Synthetic Aperture Radar (InSAR). InSAR is a powerful tool for measuring surface deformation over broad regions with sub-centimeter scale precision. In recent decades, InSAR has proven its capability to detect surface displacements caused by a variety of events such as earthquakes, ice sheet motion, volcanic activity, and subsidence (Massonnet et al., 1993; Zebker et al., 1994; Goldstein et al., 1993; Massonnet et al., 1995; Carnec et al., 1996; Fruneau et al., 1996). Despite some challenging environmental conditions (high vegetation density, steep topography, and high deformation rates) the capability of InSAR to detect landslide movements has also been demonstrated (Carnec et al., 1996; Fruneau et al., 1996; Rott et al., 1999; Vietmeier et al., 1999; Squarzoni et al., 2003; Colesanti et al., 2003; Farina et al., 2004; Catani et al., 2005). Early InSAR studies on landslides primarily used short repeat-cycle data, collected during the ERS commissioning phase in 1991 (3-day repeat cycles), or on TANDEM missions in 1995, 1996, 1997 and 1999 (1-day repeat cycles). More recent studies have utilized new processing techniques (e.g. Hilley et al, 2004) or data from new satellite systems (e.g. Kimura et al., 2000).

Little InSAR data was available for this study due to the recent launch of the ALOS satellite. To date, there are no InSAR studies published about earthflows in the Eel River basin of Northern California. The Japanese Aerospace Exploration Agency (JAXA) launched their L-band SAR system in 2006. Prior to this the primary InSAR data available was from C-band systems that perform poorly in heavily vegetated regions. There have been other L-band satellites (such as JERS), but they had limited data

availability. *Hilley et al.* (2004) was able to quantify movement of earthflows in the Berkeley vicinity of the eastern San Francisco Bay area with C-band data using an alternative processing method called PS (persistent scatterers) InSAR, which tracks persistently bright radar scatterers through time and can thus calculate displacement rates. Hilley's study took advantage of an urban setting containing many buildings with corners acting as persistent scatterers.

This study uses L-band InSAR data to identify localized landslide movement over broad regions (~100 km) while also resolving fine details in the movement of individual slides. InSAR is used to survey landslide activity in the Eel River basin of Northern California (Figure 1). Historical aerial photography data and high-resolution LiDAR topography are used to assist in the analyses and interpretation of movements at Boulder Creek. Among the various signals detected, I specifically constrain surface deformation at the Boulder Creek earthflow between February 2007 and February 2008. Boulder Creek was chosen for the study because it is optimally oriented with respect to the look direction of the satellite and exhibits measurable amounts of movement throughout the year. Displacement rates are shown to be associated with seasonal variations in rainfall. I will use these results to examine relationships between slope movement and topographic, fluvial, and lithologic properties. This in turn will help address broader questions regarding the mechanics of earthflows and the timescales on which they are active.

Figure 1. Location of the study area – northern California. The Eel and Van Duzen Rivers are drawn in blue. The Boulder Creek earthflow is labeled with the red star.

CHAPTER II

STUDY AREA AND GEOLOGIC SETTING

Geologic Setting

Persistently unstable hillslopes of the California Coast Ranges contain many active and ancient earthflows of varying sizes. The regional bedrock of the coast range is Franciscan mélange, a late Jurassic and Cretaceous age clay-rich rock unit consisting of highly sheared sandstones and siltstones in which are dispersed blocks and boulders of greenstone, chert, schist, and serpentine (Kelsey, 1978). The rocks are interpreted to represent a Mesozoic to Cenozoic aged accretionary wedge that has been uplifted and exhumed. Recent uplift (~1 mm/yr) over the past 5 Ma is driven by the migration of the Mendocino Triple Junction (Furlong and Schwartz, 2004).

The coast range of Northwestern California has a Mediterranean climate and an average annual rainfall of 0.8 m, 80% of which falls between October and April. Vegetation cover is locally variable as most slopes feature large grassland prairies separating patchy oak, madrone, and conifer forests. The highly sheared bedrock, rapid uplift, and bimodal precipitation pattern favor large landslide initiation. Both active and ancient earthflows comprise roughly 10% of this mélange area (Kelsey, 1978). The

Boulder Creek earthflow is located along the main stem of the Eel River, approximately 60 miles southeast of Eureka, California (Figure 1).

Details of the Boulder Creek Earthflow

It is important to understand the surface morphology and expected movement styles when interpreting deformation measured from space. The Boulder Creek earthflow is a large landslide complex that appears to be deforming by multiple processes, including block gliding, slumping, and viscous flow (Kelsey, 1978). No geotechnical or hydrologic data has been published for this site. Therefore, information such as depth to the water table and depth to a basal shear plane are not known. *Mackey* (personal communication) has used orthorectified aerial photographs to examine decadal movement rates at Boulder Creek. This data will be used to complement the InSAR observations. To date this appears to be the only published work that has been done at the Boulder Creek earthflow.

Anomalously large for earthflows in the region, the ~3 km^2 Boulder Creek earthflow is as large as the drainages of neighboring tributaries (Figure 2). It exhibits classic earthflow morphology as described in *Keefer and Johnson* (1983), extending from channel to ridge with a bowl-shaped accumulation zone, narrow transport zone, and bulbous toe. It is 5 km in length from the top of the accumulation zone to the bottom of the toe along the Eel River. At its widest, the accumulation zone is 3 km across. The transport zone is almost 2 km long and consistently 0.5 km wide. The toe is 1 km long and 0.75 km wide. The downslope gradient in the transport zone is oriented 240° (east-

of-north). The accumulation zone exhibits a wide range of slopes and downslope orientations due to its bowl-shaped structure.
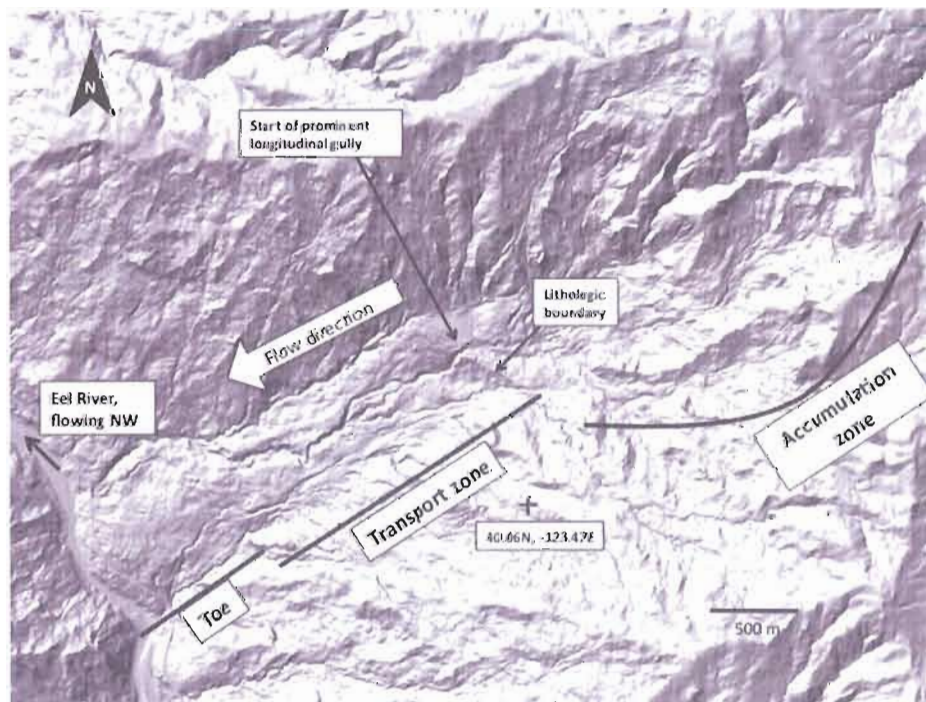
Figure 2. The Boulder Creek earthflow. Fig. 2a) Aerial photograph of the Boulder Creek earthflow. Fig. 2b) LiDAR shaded relief image of the Boulder Creek earthflow.

A prominent lithologic boundary within the earthflow appears to play a dominant role in the spatial distribution of movement. The boundary cuts obliquely across the slide (NW-SE) near the top of the transport zone (Figure 2). Above this contour there is a relatively flat bench-like region which marks the top of the transport zone. Below this line the slope becomes oversteepened (23°) for a short distance before adjusting to the slope angle of the rest of the transport zone. This strip of more resistant bedrock can be seen extending beyond the extent of Boulder Creek when looking at the bare shaded relief map created by LiDAR data in Figure 2.

Gullies have been interpreted to be a key component of sediment removal on the surface of earthflows (Kelsey, 1978; Harvey, 2001, see references therein). Boulder Creek follows the classic earthflow model in this regard with one prominent longitudinal gully extending the entire length of the transport zone as well as several smaller gullies throughout the transport and accumulation zones. LiDAR records the "central" gully to be as deep as 10 meters in places. Several smaller gullies have developed in the southern half of the transport zone, but very few in the northern half. There is also a significant gully that appears to mark the northern shear margin of the transport zone. All of these gullies deflect around the toe rather than cut through it before reaching the Eel River (Figure 2).

Earthflows extending from channel to ridge are often strongly coupled to the channel. Sometimes earthflows move when the river erodes material at the toe, essentially removing the earthflows natural buttressing (Keefer and Johnson, 1983). At other times the earthflow encroaches on, dams, or permanently pushes the river to a new

location. From observations of the shape of the river, the Boulder Creek earthflow appears to have pushed the Eel River a few hundred meters to the west. Boulder Creek resides on an outside bend of the river. This is a common location for slope instabilities due to high fluvial shear stresses on the channel margins, which can instigate bank instabilities.

CHAPTER III

DATA AND METHODS

Overview

To constrain the spatial patterns and magnitudes of movement at the Boulder Creek earthflow, I use synthetic aperture radar data from the ALOS satellite supplemented with decadal-scale historical rates derived from orthorectified aerial photographs and LiDAR data. InSAR data provides detailed information on the spatial distribution of movement over one year. Decadal-scale Boulder Creek movement is tracked using an orthorectified aerial photograph taken in 1944 and LiDAR flown in October 2006 (Mackey, personal communcation). The positions of 259 trees growing on the earthflow surface were tracked over this 62 year period to create vectors of horizontal movement. These vectors (referred to as "tree vectors") represent a historical record of magnitude and direction of Boulder Creek earthflow movement (Mackey, personal communcation). High-resolution (~1 m) topography from LiDAR data also contributes a map of terrain slope and allows for a detailed investigation of the relationships between velocity and surficial features (Figure 3).
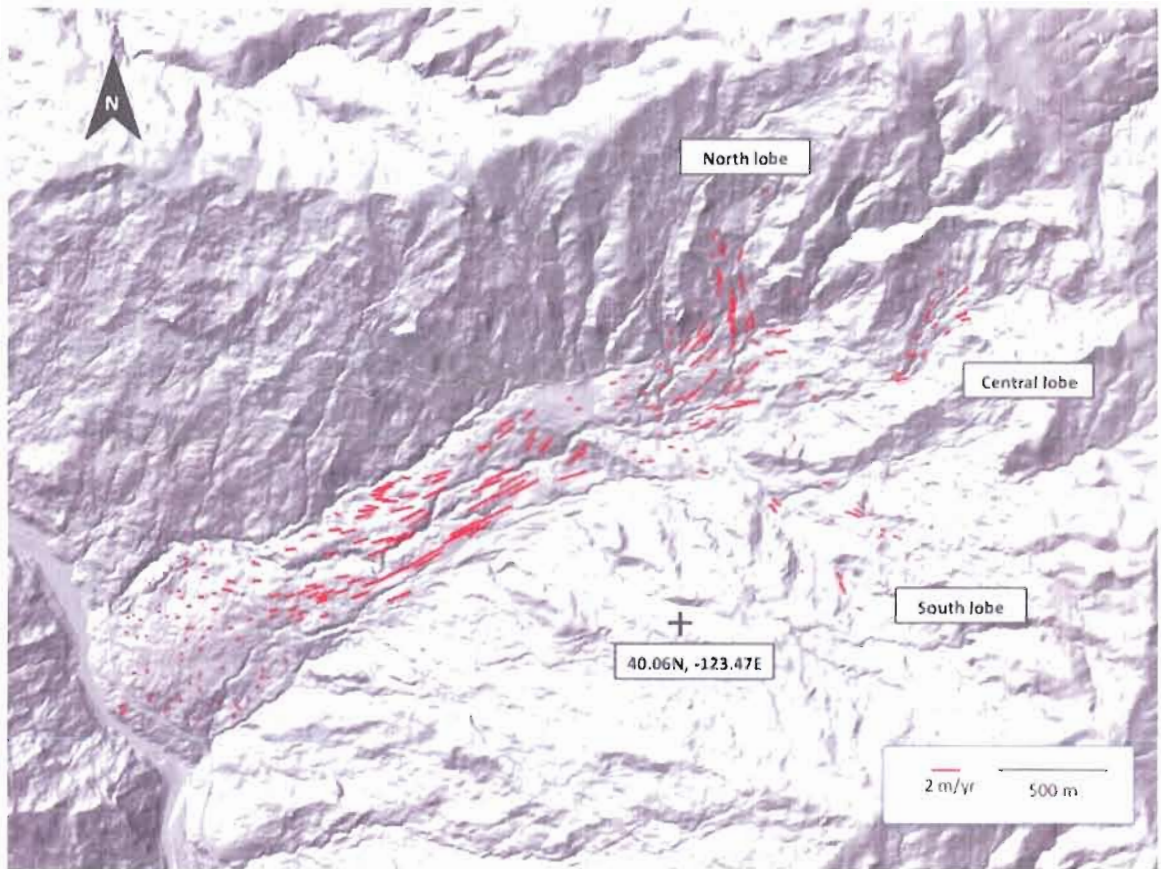
Figure 3. Tree vectors representing average yearly rates of individual trees on the surface of the Boulder Creek earthflow, tracked from 1944 through 2006. Active lobes in the accumulation zone are labeled.

InSAR Data Specifics

The ALOS satellite was launched by the Japanese Space Agency in 2006. Boulder Creek lies within the overlapping region covered by ascending satellite paths 223 and 224. The satellite line-of-sight (LOS) heading is 075° (east-of-north) with a look angle of 34.3° downward. For both paths, Boulder Creek lies within Frame 790 (Figure 4). Data are collected over the region approximately every 1.5 months. For path 223, 5 synthetic aperture radar scenes were used to make 9 interferograms spanning from March 14, 2007 to September 14, 2007. For path 224, 8 scenes were used to make 17 interferograms

spanning from February 13, 2007 through February 16, 2008 (Table 1). The availability

of data for this study was limited to a short window of time due to the recent launch of

the satellite. ERS data was also examined, but proved incoherent over the field area.
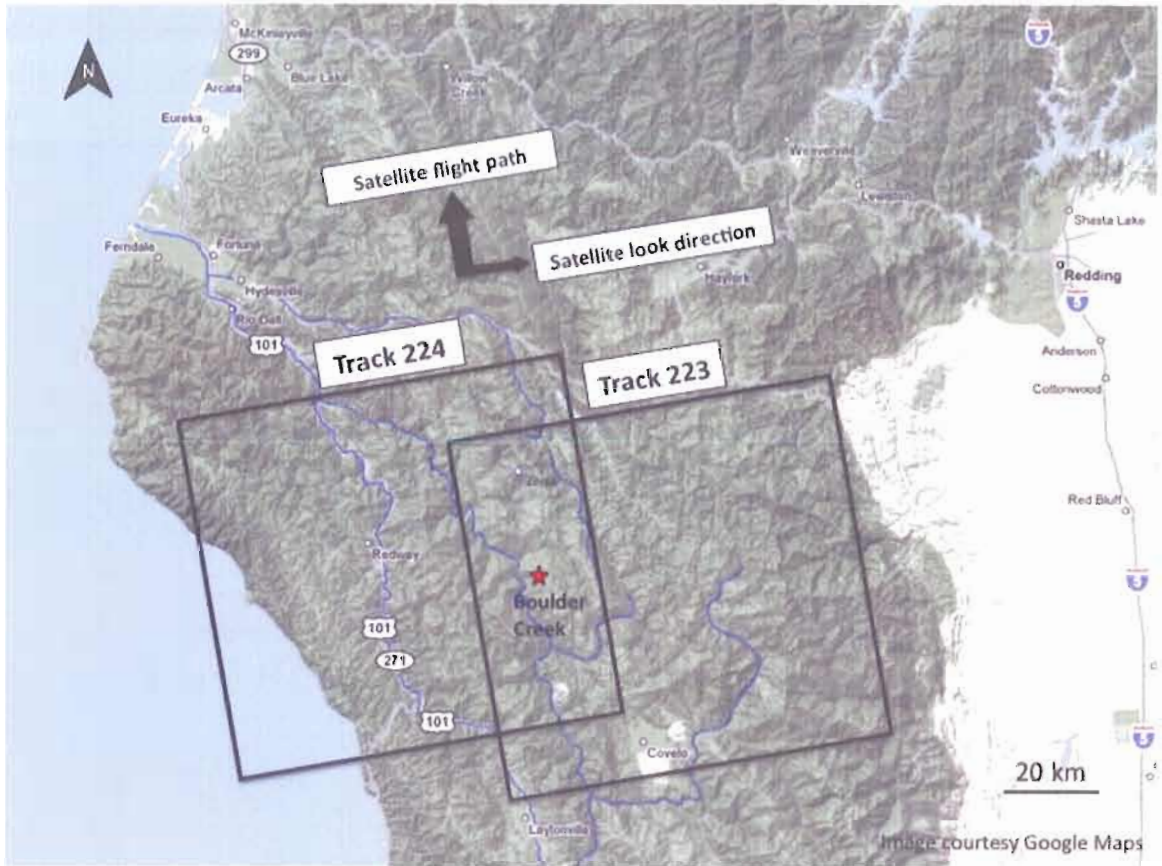

Figure 4. Location of ALOS paths 223 and 224. The Boulder Creek earthflow is located
in the overlapping region of the two tracks and labeled with a red star.

Interferogram Formation

To create an interferogram, a satellite reflects radio waves off of the earth's surface at two separate times, recording the amplitude and phase of the returning signal each time. The reflected chirps are then projected back to the individual scatters on the ground, using the Doppler shift and two-way travel time to produce a single-look complex image for each satellite pass. The two complex synthetic aperture radar (SAR) images are interfered by multiplying the first by the complex conjugate of the second (Massonnett et al., 1995). The resulting phase shift indicates the distance the surface scatterers have moved toward or away from the satellite as well as the surface height from a reference ellipsoid. By removing the topographic signal in the phase using a DEM, the surface deformation is isolated. The final step in creating an interferogram is unwrapping, which involves transforming the repeated 2π cycles of deformation into a cumulative amount of deformation. Every 2π cycle of deformation represents 11.8 cm of line-of-sight (LOS) deformation for the ALOS satellite (Massonnet and Feigl, 1998).

For this study, I processed the SAR data using the ROI_PAC (Repeat Orbit Interferometry Package) software suite developed at JPL/Caltech (Rosen et al., 2004). Raw ALOS SAR data is first converted to single look complex (SLC) images. A 1-arc second (30 m resolution) digital elevation model (DEM) collected during the Shuttle Remote Topography Mission (SRTM) is used to remove the topographic component from the phase and then the SLCs are interfered. Interferograms were processed at the standard 4-looks resolution with standard processing parameters. The displacement field obtained from my InSAR analysis continuously covers an area approximately 70x70 km^2

with a pixel resolution of ~30 meters. Line-of-sight displacement values are precise to the sub-centimeter scale.

Unwrapping Errors and Decorrelation

Phase decorrelation occurs in areas where the phase in neighboring pixels is not spatially correlated. Decorrelation is caused by low coherence, which can be quantified using the following expression:

$$\gamma = \frac{<c_1 c*_2>}{\sqrt{<c_2 c*_2><c_2 c*_1>}}$$

(1)

where c_i is the complex phase measurement for scene i, c* is the complex conjugate, and the brackets < > represent ensemble averaging. Generally, pixels of low γ are disregarded in the analysis because they do not show quantifiable evidence of deformation. Here, the decorrelated patches are used to infer locations of rapid ground movement.

Decorrelation can be caused by a number of phenomena. Anything that causes the phase to appear random or speckled, such as a change in the properties of the surface scatterers will create an incoherent patch. If the phase change across a single pixel is 2π or more, the interferometric signal also decorrelates. This can be due to steep topography, differential surface motion, or large antenna baseline (Bürgmann et al., 2000). Baseline decorrelation occurs when the satellite path for the two passes is sufficiently far apart that the orientation of the LOS look vector differs, rendering the technique's ability to detect surface deformation infeasible. All but two interferograms with a perpendicular baseline of more than 1 kilometer were not used in this study because of baseline decorrelation.

The exceptions to this baseline threshold exhibited complete coherence and fully captured the landslide signal over Boulder Creek.

Two problems were discovered during data processing. The first issue regarded the power spectral filter, which is used to remove high frequency noise from the interferograms. It was found to be dampening the landslide signal. Reducing this filter strength from the default value of 0.75 to 0.30 for most interferograms proved to preserve more of the signal during unwrapping while also minimizing the random phase speckle.

The second problem was an unwrapping error I eventually attributed to very steep deformation gradients at the margins of the transport zone. This processing error reduced and in some cases entirely removed the signal due to landslide motion at Boulder Creek but did not result in any decorrelation. By manually adjusting parameters and utilizing additional ROI PAC tools, I was able to correct the error. The error consistently occurred in a fast moving region of the transport zone. The ROI PAC scripts that unwrap the 2π cycling of the phase failed to properly integrate the phase in the areas with high displacement gradients. I discovered the problem by seeing unexpected jumps in the range change (Figure 5a). Where deformation was expected to increase (in the heart of the transport zone), it instead decreased dramatically and then resumed the expected pattern of deformation (as determined by "good" interferograms). This unwrapping error occurred in four interferograms from path 223 and six interferograms from path 224 (Table 1).

The solution for this error was to manually set the phase jump across this shear boundary. The problematic region was isolated by constructing a mask and the number of

2π phase cycles was manually assigned. The BRIDGE function within ROIPAC was used to unwrap the region with the added cycles of deformation.

The spatial extent of the region needing repair and the number of cycles to add was determined by examining pairs of short-term interferograms (with no unwrapping errors) that together span the same duration as the interferogram exhibiting unwrapping errors. The sum of the deformation from the two short-term interferograms should equal the deformation from the long interferogram. By comparing where the deformation does not correspond, the spatial extent and magnitude of unwrapping errors can be determined. (Figure 5b).
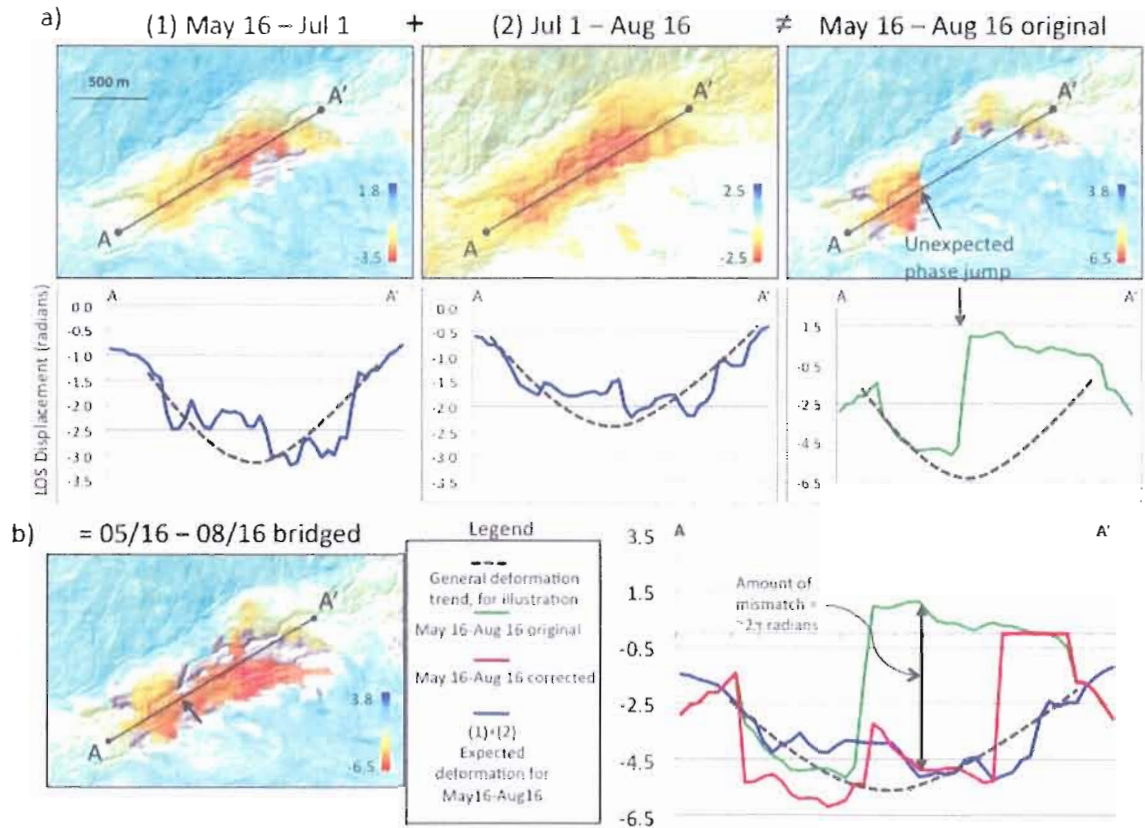
Figure 5. Example of correction for unwrapping error due to large deformation gradients in the transport zone. Fig. 5a) Two short-term interferograms, May 16 - July 1 and July 1 - August 16 (both of which do not contain the error). The total deformation over these two intervals should be equivalent to the amount of deformation in the long interferogram spanning the total duration, May 16 - August 16. Grey areas indicate where phase is decorrelated. Profiles from A to A' of displacement (in radians) for each interferogram are shown below each interferogram. The dashed black line indicates the expected trend of deformation (smooth acceleration (more negative) towards the center of the transport zone and slowing down as the edges are approached). Interferograms (1) and (2) show an expected profile of deformation. Note the unexpected phase jump in the long interferogram, altering the profile and highlighting the unwrapping error. Fig. 5b) The corrected interferogram for May 16 – August 16 is plotted after manual bridging is performed. The corrected profile is shown (in red) along with the uncorrected (green) and the expected (sum of (1) and (2)) (in blue).

Stacking Interferograms

By stacking multiple interferograms, I determine the average LOS rate of deformation over a given period of time. This method reduces noise and emphasizes features that are most consistent though time. Stacking also highlights areas with small amounts of deformation that may not be resolved using single interferograms. Stacking consists of removing the mean phase value from each interferogram. Then, pixel-by-pixel, the range change is summed and divided by the total duration of all the interferograms. For the ith pixel:

$$\Phi_i = \frac{\sum_1^n \varphi_{n,i}}{\sum_1^n \Delta t_{n,i}}$$

(2)

where Φ_i is the average phase change, $\varphi_{n,i}$ is the phase of the nth interferogram, and $\Delta t_{n,i}$ is the time span of the interferogram. If a pixel is incoherent for any one interferogram, the algorithm removes that value from the calculation.

Interferograms from different paths must be stacked separately because of the difference in look angle (33° for path 223 and 35° of path 224) (Table 1). Interferograms with a temporal baseline greater than one year are completely decorrelated and not used.

Atmospheric Artifacts

Water vapor, generally in the form of clouds or fog, can contribute significant phase artifacts (Zebker et al., 1997). Artifacts following the valleys and ridges can be seen in many interferograms, which are likely of atmospheric origin. The dimensions of

Boulder Creek, however, are much smaller than the typical dimensions of clouds (tens of kilometers) or the other long wavelength artifacts unique to single interferograms. Therefore these artifacts in any interferogram should not mask the signal of interest in a stack. However, persistent fog in valley bottoms may cause a systematic signal ambiguity near the toe of Boulder Creek unrelated to landslide deformation. All SAR data for this study was flown around 6:30am when fog often fills the Eel River valley up to tens of meters above river level, potentially altering signal strength on the toe of Boulder Creek. Since atmospheric artifacts are associated with individual SAR scenes, stacking helps to minimize the potential impact of an artifact in a given interferogram.

Projecting Line-of-sight Deformation Onto Landscape Surface

Quantifying downslope rates of the Boulder Creek earthflow are necessary in order to compare InSAR rates to tree vector rates as well as investigate earthflow dynamics, such as sediment flux rates and the role of surficial features. Because InSAR reveals only one component of the three dimensional displacement, additional constraints on the complete deformation field are needed to extract the downslope component of deformation. For this analysis, I assume that the horizontal component of deformation occurs parallel to the direction of the tree vectors. The gradient of the unit displacement vector was derived from the LiDAR data; ArcGIS was used to calculate the slope at a resolution of 60 meters. Tree vector orientations were interpolated across the earthflow at 30 meter resolution to provide the horizontal component of the unit displacement vector

(Figure 6). This calculation was performed across the slide pixel-by-pixel to allow for variations in heading and dip.

Azimuth (x- & y- components)   Surface dip (z-component)
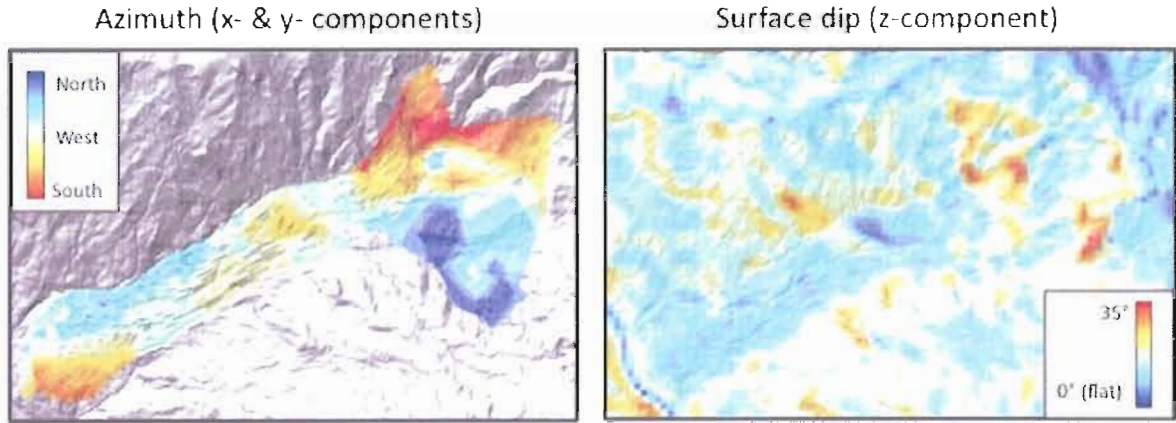
Figure 6. Azimuth and dip of downslope earthflow movement. On the left is the heading of earthflow movement derived from tree vector data. Tree vector headings were interpolated across the slide at 30m pixel resolution. The image on the right displays surface dip derived from LiDAR DEM.

The magnitude of downslope velocity was calculated using the following equation that relates LOS deformation to the complete 3D deformation field.

$$\left\| \vec{D}_i \right\| = \frac{\Delta\phi_i}{\hat{D}_i \cdot \hat{l}} \tag{3}$$

where D_i is the line-of-sight range change (from the stack), $\|D_i\|$ is the magnitude of the deformation vector at pixel i, and l is a unit vector in the direction of the satellite LOS. For each pixel, the LOS signal is projected onto the surface using the local surface dip for

the vertical component and the tree vectors for the horizontal component, creating a map of downslope velocity values averaged over the stack duration.

Time Series of Deformation

A time series of Boulder Creek deformation from February 13, 2007 to February 16, 2008 was generated from 17 interferograms on path 224 (Table 1). The algorithm (Schmidt & Bürgmann, 2003) calculates the relative change in phase between epochs for each pixel (30m x 30m) in the scene. The algorithm used to perform the time series inversion uses single value decomposition to linearly invert for the average phase change per epoch. Pixels that are decorrelated in any single interferogram are removed from the inversion. Because of significant decorrelation, the bulk of the transport zone is not included in the time series. A location in the transport zone just below the sharp break in slope was recoverable, as was the small tributary earthflow and the toe. To generate the location-specific time series plots, the phase values for a small region (90x90 meters) are averaged together for each epoch and plotted relative to another stable location in the scene. The stable location was determined by experimentation and examination of the LiDAR.

CHAPTER IV

RESULTS

Overview

In this section I present the results from 26 ALOS interferograms in the form of

stacks to examine spatial patterns of movement and a time series to explore temporal

patterns of movement as well as a look at some of the exemplary individual

interferograms. A time series inversion was performed on the path 224 interferograms to

investigate the time dependency of movement. Large deformation rates and deformation

orientation were the primary challenges to this study.

Regional Landslide Evaluation & Individual Interferogram Observations

The Boulder Creek earthflow is one of five distinct and large earthflows seen in

nearly all of the individual interferograms from path 223. The Taliaferro landslide

complex was also identified. Boulder Creek was the only apparent earthflow captured by

path 224. While this study will only investigate the Boulder Creek earthflow in detail, it

is important to emphasize the power of L-band InSAR to capture a regional view of real-

time earthflow activity in vegetated areas such as northern California. Figure 7 shows the

location and extent of the five large landslides seen in the data from satellite path 223.
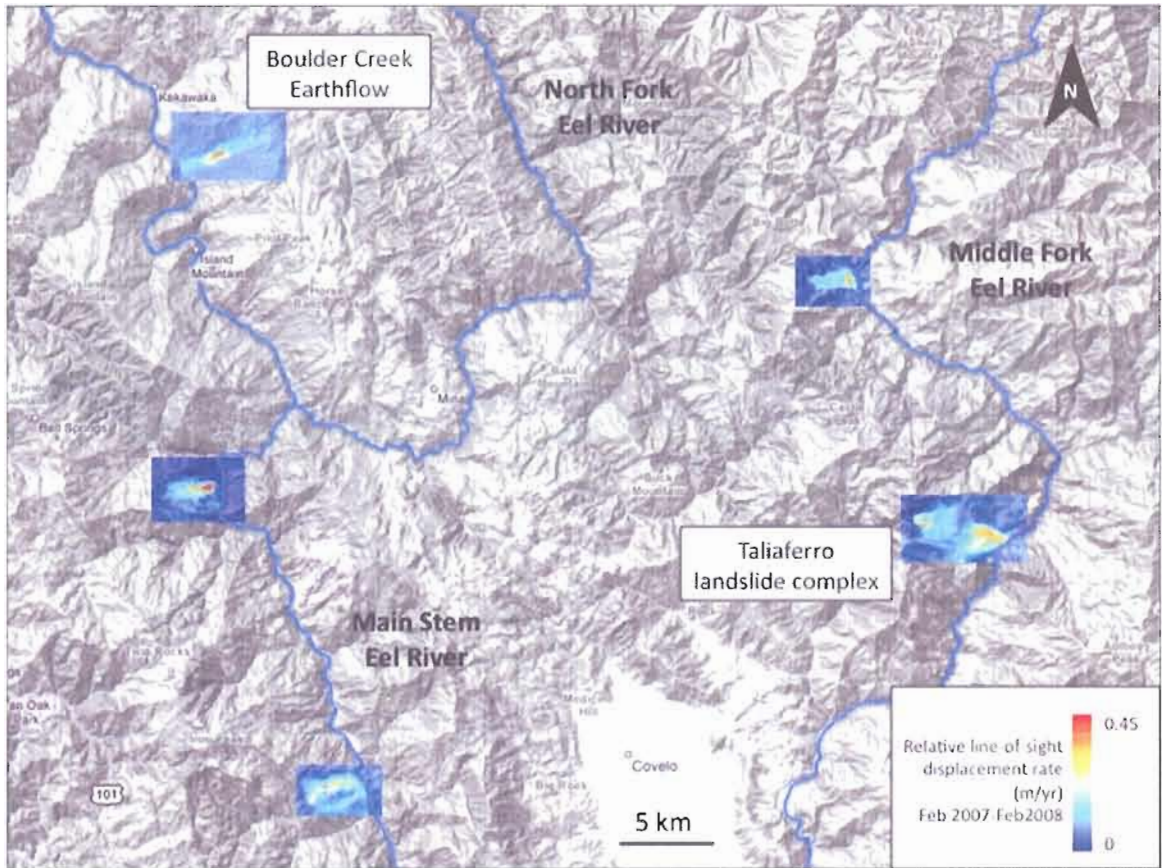
Figure 7. Regional view highlighting five earthflows found in path 223. Images are stacked using the 9 interferograms on path 223 spanning a duration of six months from March 14, 2007 to September 14, 2007.

All of the individual interferograms for this study record some amount of localized deformation at the Boulder Creek earthflow. Figure 8 presents the Boulder Creek earthflow in several individual interferograms from paths 223 and 224 highlighting various features of interest including localized signals in the transport zone and toe region, winter decorrelation due to large deformation gradients, and ideal interferograms. The nearly identical interferograms shown in Figures 8a and 8b highlight the consistent movement pattern throughout the year. Figures 8c and 8d span winter months and

highlight decorrelation (grey areas) because of the increased amounts of deformation.
Figures 8e and 8f display the localized toe signal along the Eel River and the overall
inactivity of the toe region.

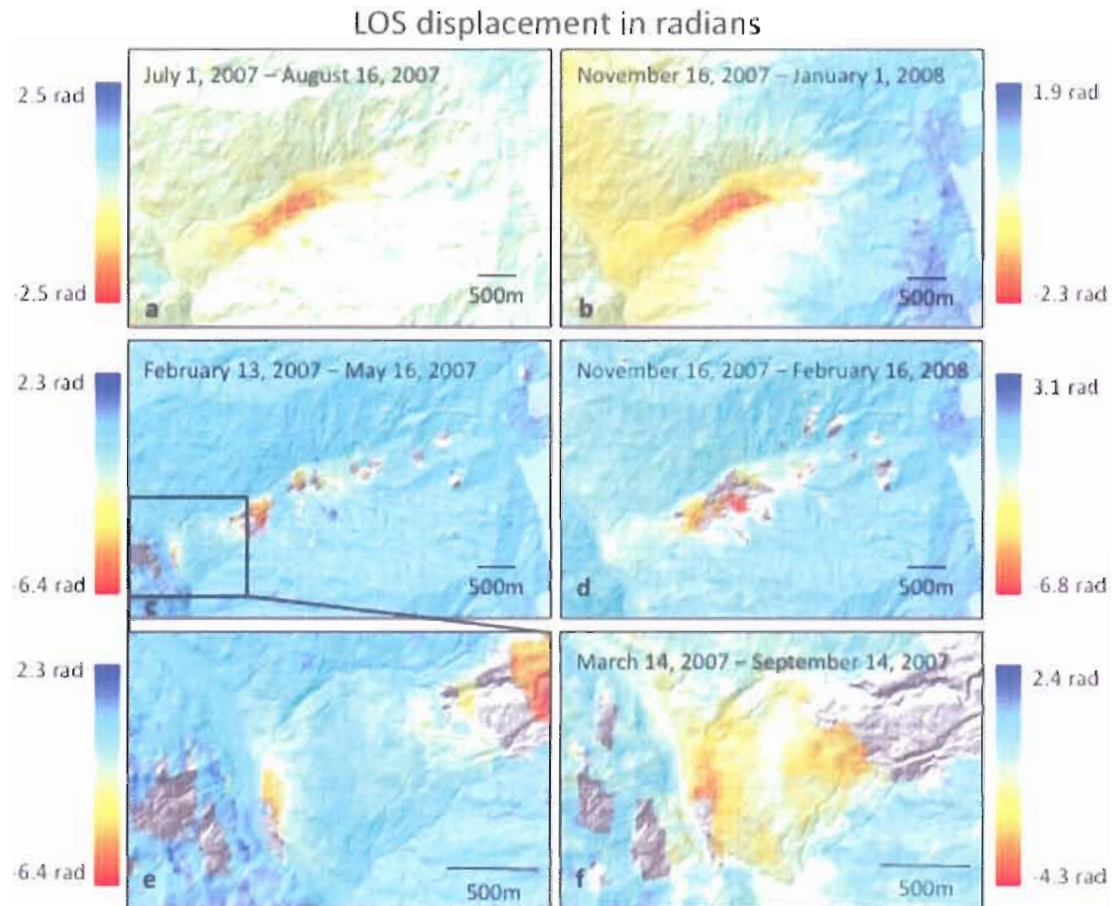Figure 8. Select individual interferograms of the Boulder Creek earthflow. Fig. 8a&b)
Exemplary interferograms with complete data coverage. These interferograms
highlight increased activity in the transport zone. Fig. 8c&d) These interferograms
show decorrelation in winter interferograms due to large amounts of deformation. Fig.
8e&f) close-up of the slump signal at the base of the earthflow, along the Eel River.

As discussed in Chapter 3, the satellite look direction is 75°east-of-north, which is nearly sub-parallel to the overall direction of flow (240°). The earthflow is traveling almost directly towards the satellite, allowing for the optimal imaging of the spatial patterns of movement at the Boulder Creek earthflow. To interpret the interferograms, one must first understand the relationship between range change measured by the satellite and deformation on the surface. Westward movement of the earthflow translates to a decrease in phase because the surface is moving closer to the satellite, reducing the range between the two. Downward movement, such as subsidence or deflation, translates to an increase in phase because the surface is moving further away from the satellite. Based on average values for the heading and dip of the transport zone, 240° and 14° respectively, 1 mm of westward movement would cancel out almost 3 mm of subsidence. The lack of additional constraints on the complete deformation field requires an assumption that all of the motion captured by the satellite is parallel to the surface. In other words, any synchronous subsidence or inflation will be interpreted as horizontal deformation. This is a small source of error and will not significantly affect interpretations of the LOS or projection results.

Detailed Examination of Boulder Creek Stacks

Interferograms are stacked over the summer months because of data availability. Nine interferograms from path 223 are stacked to generate an average summer LOS deformation rate spanning March 14, 2007 to September 14, 2007. Six interferograms from path 224 are stacked to represent a comparable rate spanning May 16, 2007 to

October 1, 2007. An average yearly rate is presented by stacking all 17 interferograms from path 224 (February 13, 2007 to February 16, 2008). For L-band InSAR with a pixel width of ~30 meters and an epoch length of 46 days, the maximum theoretical observable deformation rate is 1.3 m/yr along the satellite LOS (Calabro, 2008). The maximum LOS summer rate (~0.5 m/yr) is well below this value. The interferograms used to make summer stacks have complete data coverage with little or no decorrelation. Accelerated landslide movement occurs during wet, winter months, enough to overcome the 1.3 m/yr threshold and cause patches of decorrelation in the transport zone (Hilley et al., 2004; Iverson, 2000). Boulder Creek deformation in the dry season is observed to be well below InSAR's limit of resolving surface deformation. Covering similar periods of time and displaying nearly identical spatial patterns and rates of movement, summer stacks on paths 223 and 224 are discussed together.

Summer stacks on paths 223 and 224 image localized deformation at the Boulder Creek earthflow (Figure 9). Stacks are draped over a high-resolution hillshade image from LiDAR data to highlight surface features. Tree vectors representing historical average horizontal rates are also displayed for comparison. The light green fringe representing an average summer LOS rate of ~0.1 m/yr generally follows the morphologic boundaries of the earthflow. Beyond this fringe and off the earthflow, the blue regions represent areas of negligible movement. The maximum average LOS summer rate observed for Boulder Creek is ~0.5 m/yr, located in the transport zone. Other areas of interest include slumping at the toe margin along the Eel River, a small tributary earthflow along the south margin, and regions of continuous movement in the

accumulation zone. The spatial variation of LOS rates is in close agreement with tree

vector relative magnitudes, indicating that the relative spatial pattern of deformation is

the same over the short and longer time frame. Most notably, the regions of greatest

activity remain the same.
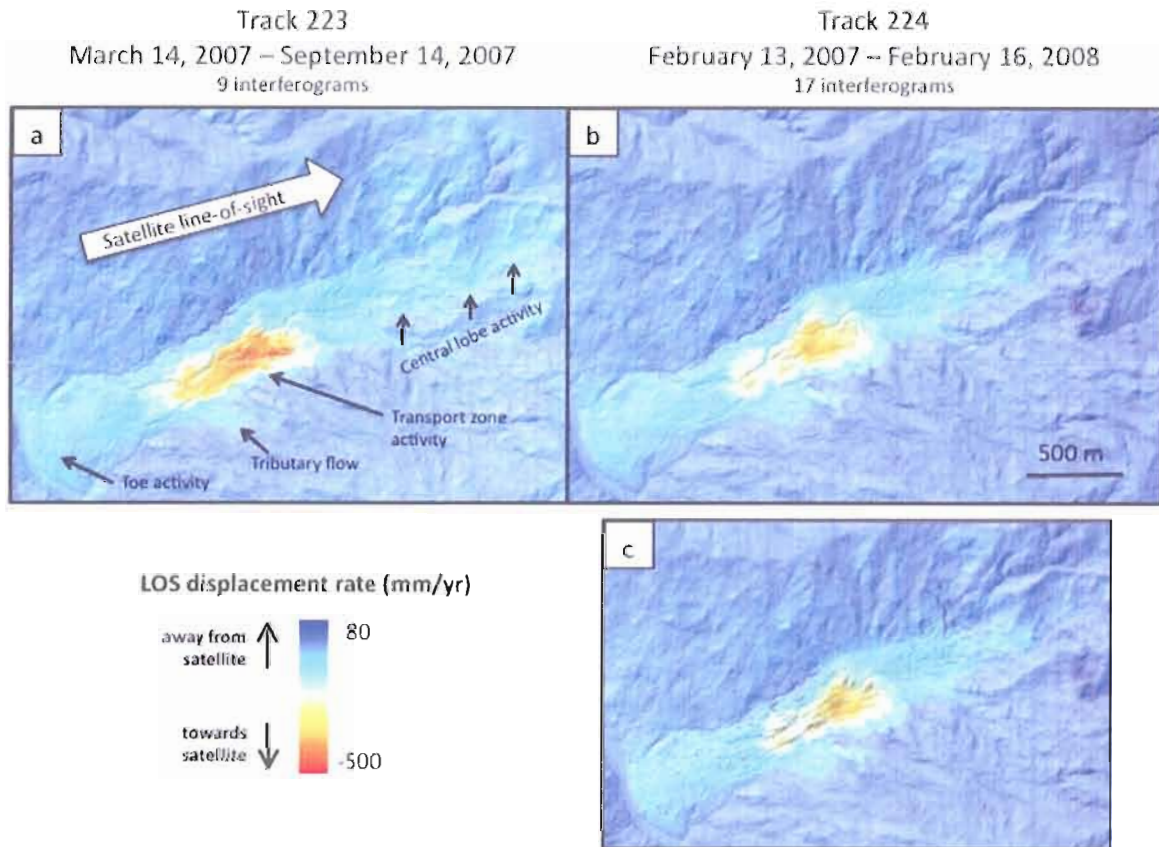
Figure 9. Stack of interferograms for satellite paths 223 and 224, representing average LOS rates (mm/yr) for the duration of the data. Fig. 9a) Stack 223 spans March 14, 2007-September 14, 2007. Fig. 9b)Stack 224 spans February 13, 2007-February 16, 2008. Fig. 9c) Stack 224 with tree vector overlay.

InSAR and the tree vectors indicate that the majority of movement in the summer

on Boulder Creek is occurring within the transport zone. The transport zone is defined as

the elongate midportion of an earthflow that connects the region of collection

(accumulation zone) with the region of deposition (toe). Flow in the transport zone is characterized as "plug" flow (Kelsey, 1978) where the material undergoes block-glide style deformation and moves downslope as a coherent unit with little internal deformation. LOS summer deformation rates are two orders of magnitude higher here than elsewhere on the slide, reaching a maximum LOS rate of ~0.5 m/yr.

A deeply incised gully (~10 m deep) bisects the transport zone. Nearly all movement in the transport zone observed by InSAR occurs within the southern "half" of the transport zone ("half" defined as the region south of the bisecting gully). Movement rates drop off steeply beyond this region. Within this region, LOS deformation rates are the highest in the center at 0.45 m/yr and decelerate towards the boundaries with rates along the gullies of ~0.3 m/yr. Additional movement beyond the borders just described occurs at rates of 0.1-0.2 m/yr.

A steep velocity gradient occurs at the top end of the transport zone. This coincides with a sharp break in slope, also called a knickpoint, where the slide surface changes from a relatively flat bench with a dip of nearly 0° to a very steep drop-off with an average slope of 23° degrees. This knickpoint is correlated to a lithologic boundary that can be seen extending well beyond Boulder Creek in the LiDAR data. Here I presume that this narrow band of more-resistant rock is responsible for the knickpoint, below which the earthflow gains speed. While there is not such a steep gradient of deformation at the bottom end of the transport zone, the green fringe representing a LOS rate of ~0.15 m/yr noticeably stops at the beginning of the toe, highlighting the corresponding change in movement with changes in surface features.

Because the tree vectors represent horizontal motion and the InSAR results reflect the component of displacement along the satellite's LOS, which is predominantly vertical, tree vector rates cannot be directly compared to LOS rates. They can, however, corroborate the spatial distribution of movement captured by InSAR. The tree vectors agree with significantly higher rates in the southern half of the transport zone. They also agree with a distinct deceleration when approaching the toe. The tree vectors highlight one region of discrepancy between the two datasets in the transport zone. Along the northern margin of the transport zone tree vectors indicate a region of westward movement that is slightly oblique to the overall direction of motion (240°). InSAR records the LOS rates in this area to be negligible. This could be due to little or no deformation during 2007 or because the motion was close to orthogonal to the satellite's look direction, as discussed more fully in Chapter 5.

The stacks highlight a small tributary flow entering the transport zone near the toe on the south side at a LOS rate of ~0.15 m/yr. There are no tree vectors to corroborate this InSAR result, however the aerial photographs used to derive the tree vectors indicate historical movement of this feature from the breakup and transport of a large rock outcrop (Mackey, personal communication).

The toe of the Boulder Creek earthflow is large, bulbous, and appears to be moving very little according to both InSAR and tree vectors observations. This classic shape for earthflow toes is representative of the region where material from the transport zone is deposited. Despite the general inactivity of the toe, a distinct InSAR signal

persists at the steep earthflow front along the Eel River. The average summer LOS deformation rate for this region is ~0.12 m/yr.

There are no tree vectors at the margin of the toe to corroborate the InSAR signal and the region may be within the zone of persistent morning fog, both of which lead to uncertainty in the interpretation of this signal. However, the signal is isolated to one portion along the toe margin and is situated directly over a fresh-looking arcuate scarp seen in the LiDAR data (Figure 8e & f). Were the signal due to fog alone, it would appear along the entire margin. This supports the interpretation that the signal is due to a localized slump. The magnitude of the signal may have been corrupted by contributions from water vapor; however, the relative change in magnitude over time can still provide insight into landslide dynamics. Another possible source of the signal is an error in the DEM, but that cannot be argued without further evidence.

The accumulation zone is a large bowl-shaped hollow where hillslope material is collected and funneled into the transport zone (Kelsey, 1978). Collection zones characteristically exhibit less continuous deformations styles such as slumping and fault block crumbling (Nolan and Janda, 1995). Little deformation is observed in the accumulation zone from InSAR data. What is observed is a relatively linear path directly in-line with the transport zone moving at LOS rates of ~0.1-0.15 m/yr. Tree-vector data for this region denote three lobes of continuous movement. InSAR activity corresponds to the central lobe of tree vector movement, however does not detect movement on the other two lobes. These styles of internal deformation are expected to cause decorrelation in the interferograms. Instead there is a spatially extensive coherent signal with negligible

magnitudes. While these non-continuous deformation styles are most likely occurring in part, the tree vectors prove that continuous deformation is also occurring within the region. The other possible reasons for the lack of InSAR movement are the wide range of slope orientations and local terrain roughness. Of the three active lobes captured by the tree vectors, only the central lobe is in-line with the satellite look direction. The north and south lobes are much closer to being orthogonal to the satellite LOS.

Downslope Velocity Projections

As described in Chapter 3, the LOS deformation rates averaged over 2007 summer months (stacks) were projected onto the slope using tree vector orientations for the horizontal component and slope derived from the DEM for the vertical component of the complete deformation field. The results of the projection can be seen in Figure 10. Using the average heading and dip for the transport zone (240° and 14°, respectively), the projection results in a downslope velocity ~3 times larger than the satellite LOS rate. Deviations from this average occur where orientations of the surface are not optimal for imaging by the satellite. This is notable along the northern margin of the transport zone where the tree vectors indicate oblique motion of ~0.5 m/yr directly towards the gully rather than straight down the transport zone. The InSAR projection, however, reports a negligible velocity along the margin.

At some locations on the slide, aspect and dip combinations approach angles that are orthogonal to the satellite LOS. This results in a singularity in the computation of the downslope velocity for a pixel. Pixels with the scaling factor $\hat{D} \cdot \hat{l}$ (from equation 3)

between -0.06 and +0.06 were removed from the calculation and do not appear in the final projection images. Recall that the satellite look direction is nearly sub-parallel to the direction of flow. This is why there are few singularities in the transport zone. Deeply incised gullies in the transport zone do, however, result in a small number of singularities because of the local terrain roughness they create. There are many singularities in the accumulation zone due to complex surface morhpology and the wide range of slope orientations. These singularities result in low data coverage for the region. Because InSAR captured so little movement in the accumulation zone it was already a poor candidate for the projection. Therefore the downslope projection is most appropriate for the transport zone and toe region of Boulder Creek.
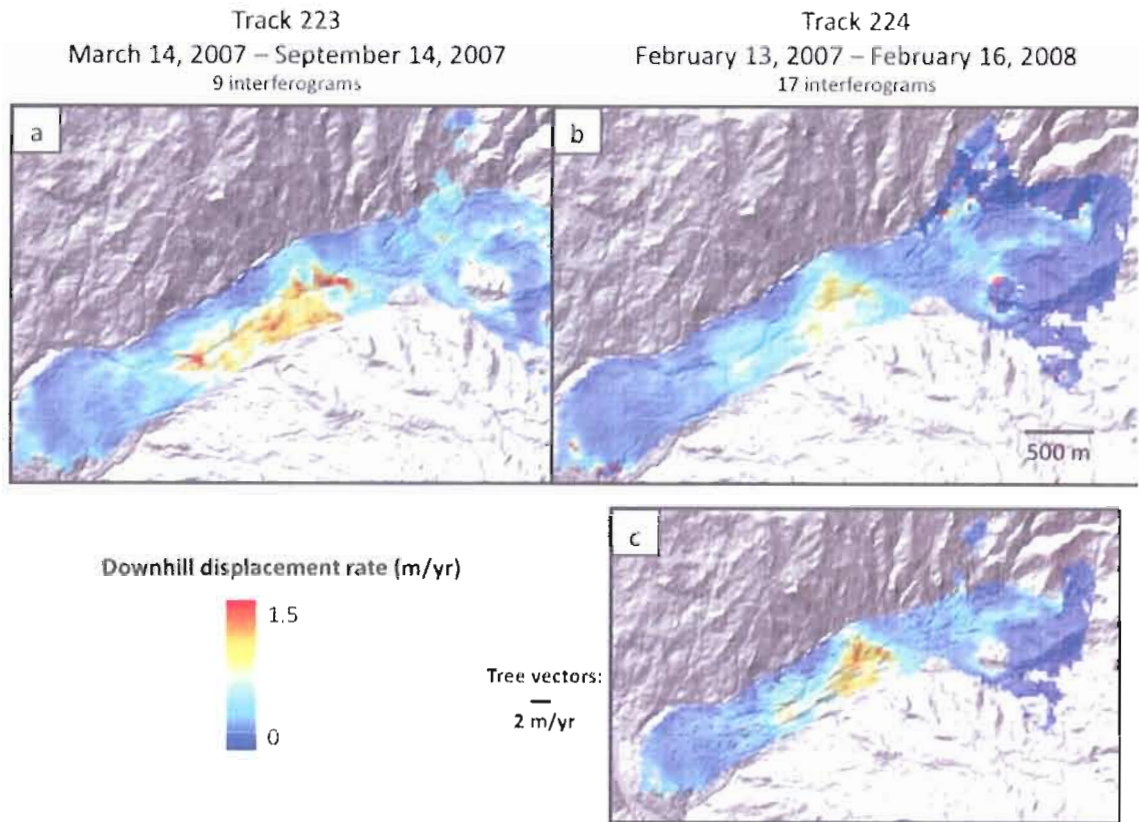
Figure 10. Downslope velocity projections for each stack. Colorscale saturated at 0 and 3 m/yr. Values below 0 m/yr appear a deep blue. Values above 3 m/yr appear red. These extreme values are interpreted to be artifacts of the projection due to complex surface morphology and are not physically representative. This projection is most relevant for the intermediate values found in the transport zone. Fig. 10a) Downslope velocity for path 224. Fig. 10b) Downslope velocity for path 224. Fig 10c) Downslope velocity for path 224 with tree vector overlay.

The downslope velocity values from InSAR range from 0.5 to 1.5 m/yr in the transport zone and ~0.3 m/yr elsewhere. Tree vectors for this region measure 2.0 to 2.5 m/yr in the transport zone and ~0.5 m/yr elsewhere. As the InSAR-derived rates are for summer only on path 223 and weighted towards the summer months on path 224 (due too loss of coherence in the transport zone in winter interferograms), it is expected that they will be lower than the tree vector rates, which record yearly averages including accelerated movement in the winter. Tree vector rates are consistently around 2 times

larger than the InSAR-derived summer rates, thus corroborating the InSAR projection results.

Seasonal Signal

A strong seasonal signal can be seen in all regions of the earthflow included in the inversion (Figure 11). Rates of movement are plotted in millimeters per day and represent an average rate for the given epoch. All epochs are 46 days except for the first, which is 92 days. Movement decelerates in the spring of 2007 in concert with the rain. The earthflow is still slowing down in October 2007 when the winter rains begin again. It is not until the beginning of January 2008 that the earthflow begins to accelerate. This ~2 month lag can be seen in all three locations plotted in Figure 11, however the magnitude of movement lowers by an order of magnitude as you progress from the transport zone to the small tributary flow to the slumping signal at the toe margin. The transport zone (Figure 11, red diamonds) reaches a peak rate of 1.2 mm/day (0.44 m/yr) in June 2007 and then steadily slows down to 0.5 mm/day (0.18 m/yr) by the end of December. At this point the transport zone begins accelerating again to a final rate of 0.75 mm/day (0.27 m/yr). This same pattern of deceleration is seen in the small tributary flow entering the transport zone near the toe (green diamonds), however its fastest rate is 0.3 mm/day and slows to nearly zero by the end of the year. The toe slump (yellow diamonds) also shows a dampened but consistent pattern of maximum speed in June and slowing to nearly zero before beginning to accelerate again in 2008.
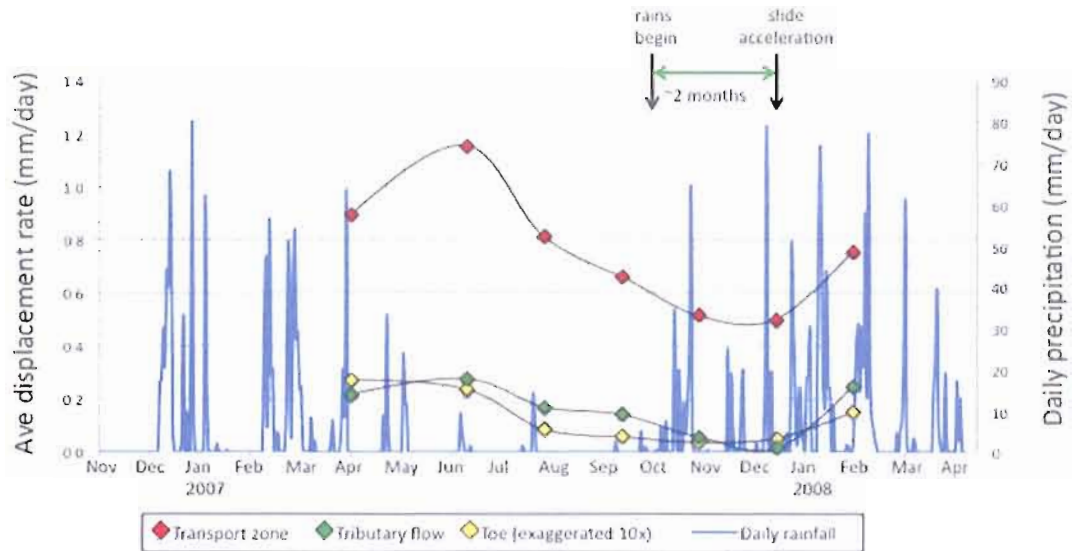
Figure 11. February 2007 to February 2008 time series of average daily velocities for three regions of the Boulder Creek earthflow. Daily rainfall collected at the Zenia meteorological station, approximately 15km north of Boulder Creek, is plotted in blue. The red diamonds represent movement in the transport zone. Green diamonds represent a location in the tributary flow and yellow diamonds represent movement at the margin of the toe.

CHAPTER V

DISCUSSION OF RESULTS

Overview

In the previous chapter, I analyzed ALOS satellite data in conjunction with historical movement rates and LiDAR data in an effort to constrain spatial and temporal patterns of movement at the Boulder Creek earthflow. In this chapter, I discuss the implications of interpreting landslide movement measured in the satellite LOS as well as how patterns of surface movement through space and time relate to earthflow morphology and dynamics.

Investigating the Spatial and Temporal Variations in Velocity

The downslope velocity projections represent earthflow movement averaged over one year, from February 13, 2007 to February 16, 2008. While the projections are estimates of downslope velocities and do not consider synchronous vertical signals (such as uplift or subsidence of the surface), they provide a first order map of where and how much the earthflow is moving over one year. The following sections first discuss the spatial variability of velocities averaged over one year and then the temporal variability within that year. The spatial variability highlights connections between lithology and

gullies and surface movement. Temporal variability highlights seasonal patterns of movement that correlate with rainfall.

The spatial variability of downslope velocities determined from the InSAR data highlight distinct zones of activity within the earthflow. Movement is predominantly occurring in the transport zone with minimal activity seen in the accumulation zone and toe regions. Between this "hot spot" of activity and the Eel River is a relatively inactive toe, prompting the question of what is driving movement. It is often speculated that earthflow movement is driven by erosion at the toe by the channel below. The inactive toe of Boulder Creek indicates that stresses are not being transmitted upslope from the Eel River. Further, the slump at the toe margin does not appear to have any effect upslope.

From examining the LiDAR, it appears possible that the earthflow is driven from above by material collected in the accumulation zone and funneled into the transport zone. A lobe of material can be seen approaching the sharp break in slope near the top of the transport zone. I interpret this to suggest a more episodic supply of material to the transport zone; when enough material collects it forms lobes with enough force from above to advance over the flat bench top and enter the transport zone conveyor belt.

With an inactive toe, gullies appear to be the primary mechanism connecting the channel to the transport zone. Several deep gullies (<15 m) dissect the fastest regions of the transport zone. Downslope, the gullies coalesce and wrap around both sides of the toe before merging with the Eel River. It is also notable that the gullies are absent from the slow regions of the transport zone (the northern half). This suggests that the locations

of gullies can be associated with regions of activity and that gullies play a large role in the removal of sediment from the earthflow. Erosion from gullies has been found to be a significant contributor for sediment flux in channels over short and long term (Harvey, 2001; Betts et al., 2003).

In addition to the accumulation zone, a smaller amount of material enters the transport zone from the tributary earthflow. This region, too, abuts the locked toe region and again gullies appear to be responsible for transporting that material off the earthflow. A deep gully forms immediately downslope from where the tributary flow enters the transport zone, again implying a direct relationship between gullies and regions of activity and sediment removal.

The rapid increase in velocity after the sharp break in slope near the top of the transport zone provides insight into the depth and shape of the Boulder Creek earthflow. This velocity increase is most likely due to the lithologic boundary discussed in Chapter 4. Above this boundary the surface is relatively flat and immediately below it the surface dips steeply, up to 23°, for ~100 meters before leveling out to the average transport zone dip of ~14°. Because of the broad extent and sharp linearity of the feature, this lithologic boundary is likely to have persisted through much of Boulder Creek's history and appears to largely control the location of the top of the transport zone. *Coe et al.* (2008) determined that when landslides have moved distances larger than the dimensions of the largest basal topographic irregularities, landslide surface morphology can be used as a guide to the morphology of the basal slip surface. Due to its large size and significant amounts of deformation over historic timescales (~150 meters in 64 years according to

tree vectors), I assume that such an argument about surface morphology mimicking a basal slip surface is relevant for Boulder Creek, at least locally in the upper reaches of the transport zone. The prominent knickpoint suggests that bedrock is close to the surface at that location, which would mean that the earthflow is quite thin there. Transport zone thickness cannot be determined, however, fast-moving flows are often less thick than slower ones of the same surface area in order to balance the amount of material entering and leaving the region. This suggests a gradual thickening just below the knickpoint to some thickness which is most likely maintained along the transport zone.

Individual interferograms of Boulder Creek provide information on seasonal variations in rates and styles of movement. Interferograms spanning summer months show continuous data coverage and lower rates than winter months (Figure 8a & b). Small patches of decorrelation in interferograms spanning winter months are attributed to large amounts of deformation or internal deformation (Figure 8c & d) (Calabro, 2008). Because of the high precipitation in the winter, this is when the earthflow is expected to move most rapidly. Decorrelation patches occur in regions where the most activity is expected: over gullies in the transport zone.

The time series of range change explores the relationship between precipitation and slide movement. Despite the drastic spatial variability in velocities, the time series highlights a similar temporal pattern across the slide which correlates strongly with seasonal rainfall patterns. Figure 11 plots average LOS velocities (mm/day) at different locations on the earthflow along with daily rainfall data collected by the California Department of Water Resources at the Zenia meteorological station, approximately 15

km north of the study site (Figure 1). While the magnitudes of the rates are not directly applicable because they are in the LOS and not downslope, the relative change provides insight into seasonal patterns. To the first order, it can be seen that as the rains begin in October 2007, the earthflow is still decelerating. However, about 2 months later, at the beginning of January, the earthflow begins to accelerate. I interpret this to be a delayed response to rainfall, which would suggest that the Boulder Creek earthflow is hydrologically driven. As the water table rises, pore pressures and sliding velocities increase. When the water table lowers, pore pressures and sliding velocities decrease (Ehlig, 1992). *Iverson* (2000) describes the relationship between sliding rate and time since rainfall onset. The diffusion of pore pressure through the slide decreases the normal force and frictional resistance, thereby allowing the slide to accelerate. As pore pressure diffuses through the slide there is a lag between the onset of rainfall and the acceleration of the slide. The relatively long lag time of ~2 months could indicate low diffusivity for the earthflow, perhaps caused by the clay-rich material or a deep basal shear zone (Keefer and Johnson, 1983.

Despite being much larger than most documented earthflows in the region, Boulder Creek appears to be similar in its rates and styles of movement. Velocities in the transport zone of Boulder Creek approach a yearly average of 2 m/yr. Elsewhere on the slide velocities range from 0 – 1 m/yr. Earthflow velocities at other field sites have been observed to range from 0.5 m/yr to 6 m/yr with occasional surges of tens of meters in a matter of days. The Minor Creek earthflow in northwestern California was monitored from 1982 to 1985 (Iverson and Major, 1987). This 800 meter-long earthflow has a

summer creep rate of 1-4 mm/yr and accelerates up to 0.5 m/yr in the winter.

Acceleration into winter rates occurred between November and March depending on the

year. Rapid movement persisted into May or June. The inconsistent delays between onset

of seasonal rainfall and onset of rapid movement at different field sites highlight the

episodic nature of earthflow movement. *Hilley et al.* (2004) observed a lag of ~3 weeks

for earthflows in the East Bay Hills region near San Francisco, California. These

earthflows are ~1 km long and move 27-38 mm/yr downslope, as inferred from InSAR

range change. The Portuguese Bend landslide (~1 km^2) on the Palos Verdes peninsula

near Los Angeles, California, shows a lag of approximately 1 month. Due to extensive

monitoring, the depth of this earthflow is known to be 18 meters on average (Calabro,

2008). The fact that rates and styles of deformation observed at Boulder Creek are

consistent with other earthflows in the area suggests that L-band InSAR can successfully

characterize and quantify landslide-related deformation.

Investigating InSAR Line-of-sight sensitivity

The previous sections and Figure 7 highlight the power of L-band InSAR to

identify and quantify earthflows in the vegetated terrain of Northern California. Prior to

the introduction of this broad remote sensing tool, earthflows were found and studied on

a case-by-case basis. Five large earthflows were identified using InSAR in this study,

thus providing a "snapshot" of real-time regional earthflow activity in the Eel River

basin. An understanding of the limitations that come with measuring deformation using a

single look direction is important, but even one component of deformation is enough to

highlight areas of interest and infer relationships between surface deformation and earthflow morphology and dynamics.

There are a number of limitations that must be considered when interpreting InSAR data. The largest error source comes from atmospheric artifacts. Other than the possible fog signal at the base of the earthflow, no significant atmospheric artifacts appear to be present in any interferograms. Limited temporal sampling, the inability to see a signal in long-duration interferograms because of high rates, and no descending data are additional limitations of this study. Temporal sampling is, on average, every 46 days for this dataset, which is the best that can be attained for the ALOS satellite orbit.

InSAR's sensitivity to the orientation of deformation is highlighted in this study. Deformation orthogonal to the LOS will go undetected because the interferometric analysis is insensitive to motion in this direction. The transport zone of Boulder Creek is optimally oriented for imaging by an ascending InSAR satellite because surface motion is heading nearly sub-parallel to the satellite look direction. The accumulation zone, on the other hand, exhibits greater variability in the orientation of surface movement, and the regions where the expected movement is orthogonal to the LOS show no signal in the interferograms. The toe region is extremely smooth and the direction of motion is generally in-line with the transport zone, making it another optimal region for InSAR imaging. The following sections compare ascending InSAR data (Figure 9) to horizontal rates derived from aerial photography to investigate what parameters (i.e. deformation orientation, surface roughness) are most important or limiting when interpreting earthflow movement using InSAR.

While the average LOS rates represent only one component of the total movement of the Boulder Creek earthflow, they do provide a sufficient level of detail with which InSAR can resolve landslide-related deformation. Tree vectors could only be created where trees persist on the earthflow through time. As seen in figure 3, tree vector coverage is relatively dense across the earthflow, highlighting specific and interesting regions of activity such as viscous-flow characteristics in the southern half of the transport zone and oblique movement near the northern margin of the transport zone. Tree vectors are absent from the tributary flow, where no trees were able to be tracked. Despite a lack of trees, boulders and shrubs could be seen moving downslope through time indicating activity of this feature (Mackey, personal communication). In the following sections I compare spatial patterns of movement detected by InSAR and the tree vectors.

The extraordinary detail that can be seen in the transport zone highlights why Boulder Creek was chosen to be the subject of this study. The movement in this region is heading nearly sub-parallel to the satellite look direction, resulting in the satellite detecting as much movement as possible. While the other earthflows identified in this study also demonstrate internal displacement gradients, the large size of the transport zone of Boulder Creek combined with its optimal orientation provide the best resolution with which to study earthflow movement. Prominent displacement gradients appear consistently in all of the individual interferograms highlighting the steady pattern of movement. The margins of movement seen by the satellite coincide well with the interpreted geomorphic boundaries of the slide. Similar to what is seen at Boulder Creek,

the transport zones at the Kekawaka and Halloween earthflows (see Figure 1; Halloween Earthflow along the Van Duzen River) also show a similar style of deformation where material moves as a coherent unit downslope (Mackey et al., 2009; Kelsey 1978). This style of continuous deformation is ideal for detection by InSAR because of the small amounts of internal rotation and shear that could otherwise result in too much change in the surface scatterers and cause decorrelation.

Limitations in resolving deformation that is oblique to the LOS is more apparent in the accumulation zone. This bowl-shaped collection zone takes material from near the ridges where gradients are higher, and funnels the material downslope and inward towards the top of the transport zone. Tree vectors indicate three discrete active lobes of material moving downslope from prominent headscarps towards the transport zone: a central lobe moving relatively parallel to the transport zone and a lobe on either side (referred to as the "north" lobe and the "south" lobe), each approximately 30° off the central lobe heading (Figure 3). The InSAR data captures distinct movement of ~0.13 m/yr (LOS) in the central lobe that nicely agrees with the location of tree vectors, which record horizontal rates of 1-2 m/yr. The north and south lobes, however, appear to be inactive according to the InSAR data, but very active according to the tree vectors. Tree vectors indicate that the north lobe is the most active of the three with horizontal rates ranging from 0.5 to 1.5 m/yr. I attribute the difference between agreement in the central lobe and disagreement in the north and south lobes to InSAR's dependence on the orientation of deformation relative to the LOS look direction. Deformation in the central

lobe is optimally oriented with respect to the satellite while the north and south lobes are approaching orthogonality to the LOS.

I assume discontinuous deformation to be another challenging parameter when landslide-related movement in the accumulation zone. Deformation styles commonly observed in collection zones of earthflows, slump blocks, rotation, tension cracks, and crumbling, result in small-scale surface roughness. Rapid movement and small-scale rotations from crumbling and rolling material is expected to cause decorrelation in the interferograms. While the magnitude of LOS deformation is negligible for the north and south lobes, there remains a spatially extensive coherent signal across the region. The fact that there is always a coherent signal across the accumulation zone indicates that deformation is either not occurring or, in the central lobe at least, occurring in a continuous fashion. This is corroborated by the tree vectors, which highlight continuous movement in all three lobes. Thus, it appears that the complex surface morphology is not an impediment to using InSAR in this locality. Spatial averaging during processing and continuous flow-like motion in the area provides coherent data cross the zone.

As discussed in Chapter 4, an interesting phase signal resides at the steep margin of the toe along the Eel River. This localized signal (~200x100 meters) must be interpreted with caution because of the possible water vapor contribution to the phase. A signal attributed to fog does not appear in every interferogram but it does appear in both stacks, indicating that it is a persistent signal. While the magnitude of the signal may be questionable, the location of the signal proves that it can be attributed to landslide-related motion. Not only is the signal unique to a small section of the margin, but the LiDAR

data highlights a fresh arcuate shape in the same location as the InSAR signal. Were the signal to be due solely to fog, it would extend across the entire margin (Figure 8e & f).

While LOS displacement rates in the transport and accumulation zones are assumed to be primarily horizontal, I assume the slump signal to be predominantly vertical. A rotational slump would likely result in the surface moving downward. Because the majority of the toe is not moving at all, horizontally or vertically, as indicated by InSAR and the tree vectors, it is unlikely that the signal of interest would be moving horizontally. This assumption holds when considering the expected direction of range change for downward vertical motion. Positive range change indicates that the surface is moving away from the satellite. This can be interpreted as downslope surface-parallel movement or subsidence/deflation of the toe margin. The range change observed for the toe slump, however, is negative. This indicates some form of uplift. Folding and multiple shear surfaces due to compression from upslope could result in uplift of the toe margin. Further investigation of this feature is necessary, however, to validate the signal. It is also possible that fog has affected the signal.

The magnitude of the signal may have been corrupted by contributions from water vapor and is therefore not directly applicable. I assume the fog to behave as a volumetric scatterer of the satellite signal. Properties of the fog that could affect the phase signal, such as thickness, density, and mere presence, can vary from day to day. The calculated phase change along the river could be reflecting changes in the fog parameters rather than changes in the surface. The time series discussion later in this chapter, however, highlights a seasonal variation in displacement for this feature that is identical to patterns

elsewhere on the slide. While this also is an argument for the validity of the signal, it does not necessarily defend the magnitudes. Further investigation would be required to gain confidence in this result.

CHAPTER VI

SUMMARY AND CONCLUSIONS

This study of the Boulder Creek earthflow has incorporated InSAR, aerial photo

analysis, and LiDAR in an attempt to monitor the slide and better understand its

dynamics. Two-pass L-band satellite interferometry is used to determine deformation

rates during the summer months of 2007. The downslope velocity values range from 0.5

to 1.5 m/yr in the transport zone and ~0.3 m/yr elsewhere. A comparison is made

between these results and horizontal rates derived from orthorectified aerial photographs

and LiDAR spanning 1944-2006. Tree vectors for this region measure 2.0 to 2.5 m/yr in

the transport zone and ~0.5 m/yr elsewhere. Tree vector rates are consistently ~2 times

larger than the InSAR-derived summer rates. Because tree vector rates represent yearly

averages, which include accelerated winter movement, and InSAR rates are for the

summer only, these results are in agreement.

My results highlight the ability of L-band InSAR to identify and quantify

earthflow activity in highly-vegetated terrain. Five large earthflows (including Boulder

Creek) are identified in one frame, providing a snapshot of earthflow activity for a 70km

x 70 km region. Within the borders of the Boulder Creek earthflow, InSAR images

spatial heterogeneities of movement at high spatial resolution (30m x 30m). The most

displacement occurs in the transport zone with less activity seen in the accumulation and toe regions. Within the transport zone, the regions of highest displacements are seen to correlate with the regions of highest gully density, suggesting that gullies either form in response to or are the cause of increased surface movement. If they are the cause of movement, is movement only happening as deep as the gully thalwegs? Perhaps this creates a positive feedback loop where the gullies remove enough material to lessen the normal load on the basal shear plane and accelerate movement of the whole unit. If gully incision is a response to movement, then perhaps the activity breaks up the surface and encourages channel formation, which would then continue to assist in moving material. A sharp break in slope attributed to a lithologic boundary appears to dictate the start of the high displacements of the transport zone.

The time series inversion for path 224 interferograms displays variations in LOS rates between February, 2007 and February, 2008. All regions of the slide show a significant deceleration from March 2007 through December 2007 before beginning to accelerate in January 2008, approximately 2 months after the winter rains began. This relatively long phase lag between the onset of rain and the onset of increased earthflow activity could help to constrain physical parameters of the slide such as diffusivity and depth to a basal shear zone.

This study examined limitations to the interpretation of InSAR results derived from a single look vector. InSAR is shown to be sensitive to the orientation of the deformation such that significant amounts of deformation go unseen if moving orthogonal to the satellite line-of-sight. Such is the case in the accumulation zone of the

Boulder Creek earthflow, where only one of three lobes of activity observed by the tree vectors is observed by InSAR.

The study of the Boulder Creek earthflow could be furthered by traditional site-specific methods such as surveying, boreholes, and stake lines as well as GPS and additional InSAR data. This would expand temporal data coverage, constrain vertical signals, verify the spatial extent of movement in the accumulation zone, constrain the large winter rates in the transport zone which InSAR could not, and investigate the toe margin "uplift" signal.

APPENDIX A

LIST OF INTERFEROGRAMS USED

Path	Starting Scene	Ending Scene	Baseline (m)	Bridge required?
223	2007 March 14	2007 April 29	-571	-
223	2007 March 14	2007 June 14	-139	Yes
223	2007 March 14	2007 September 14	-878	Yes
223	2007 April 29	2007 June 14	431	-
223	2007 April 29	2007 July 30	62	Yes
223	2007 April 29	2007 September 14	-333	Yes
223	2007 June 14	2007 July 30	-369	-
223	2007 June 14	2007 September 14	-765	Yes
223	2007 July 30	2007 September 14	-395	-
224	2007 February 13	2007 May 16	-670	Yes
224	2007 February 13	2007 July 1	-775	-
224	2007 May 16	2007 July 1	3140	-
224	2007 May 16	2007 August 16	-290	Yes
224	2007 May 16	2007 October 1	-747	Yes
224	2007 July 1	2007 August 16	-277	-
224	2007 July 1	2007 October 1	-640	-
224	2007 July 1	2007 November 16	-810	Yes
224	2007 July 1	2008 January 1	-916	-
224	2007 August 16	2007 October 1	-455	-
224	2007 August 16	2007 November 16	-620	-
224	2007 August 16	2008 January 1	-730	Yes
224	2007 October 1	2007 November 16	-170	-
224	2007 October 1	2008 January 1	-275	-
224	2007 November 16	2008 January 1	-105	-
224	2007 November 16	2008 February 16	-1065	Yes
224	2008 January 1	2008 February 16	-960	-

APPENDIX B

GLOSSARY OF TERMS

ALOS: Advanced land observation satellite

ERS: European Remote Sensing satellites

GPS: Global Positioning System

InSAR: Interferometric Synthetic Aperture Radar

JAXA: Japan Aerospace Exploration Agency

JERS: Japanese Earth Resources Satellite

LiDAR: Light Detection And Ranging

LOS: Line of Sight

SAR: Synthetic Aperture Radar

REFERENCES

Betts, H.D., Trustrum, N.A., and De Rose, R.C. (2003). Geomorphic changes in a complex gully system measured from sequential digital elevation models and implications for management. *Earth Surface Processes and Landforms*, 28, 1043-1058.

Burbank D.W., Leland, J., Fielding, E., et al. (1996). Bedrock incision, rock uplift and threshold hillslopes in the northwestern Himalayas. *Nature,* 379, 505-510.

Burbank, D.W. and Anderson, R.S. (2001). *Tectonic Geomorphology*. Blackwell Science Ltd.

Bürgmann, R. et al. (2000). Synthetic aperture radar interferometry to measure Earth's surface topography and its deformation. *Annual Reviews of Earth and Planetary Sciences,* 28, 169-209.

Calabro, M.D., 2008. *An examinatino of surface displacement at the Portuguese Bend landslide, southern California, using radar interferometry*. Unpublisehd Master of Science thesis, University of Oregon, Eugene, Oregon.

Carnec, C., Massonnet, D., and King, C. (1996). Two examples of the use of SAR interferometry on displacement fields of small spatial extent. *Geophysical Research Letters*, 23, 3579– 3582.

Catani, F., Farina, P., Moretti, S., et al. (2005). On the application of SAR interferometry to geomorphological studies: Estimation of landform attributes and mass movements. *Geomorphology,* 66, 119-131.

Colesanti, C., Ferretti, A., Novali, F., et al. (2003). SAR Monitoring of Progressive and Seasonal Ground Deformation Using the Permanent Scatterers Technique. *IEEE Transactions on Geoscience and Remote Sensing*, 41(7), 1685-1701.

Cruden, D.M. and Varnes, D.J. (1996). *Landslide types and processes*. In Turner, A.K. and Schuster, R.L. (eds.), Landslides--Investigation and Mitigation. Washington

D.C., National Academy Press, Transportation Research Board Special Report 247, 36-75.

Farina, P., Colombo, D., Fumagalli, A., et al. (2004). On the integration of remote sensing data within landslide risk analysis. *International Geological Congress, Abstracts*, 32(2), 183.

Fruneau, B., J. Achache, and C. Delacourt (1996). Observation and modeling of the SaintEtienne-de-Tinee landslide using SAR interferometry. *Tectonophysics,* 265, 181-190.

Fuller, C. W., Willett, S. D., Hovius, N. and Slingerland, R. (2003). Erosion rates for Taiwan mountain basins: New determinations from suspended sediment records and a stochastic model of their temporal variation. *Geology*, 111, 71–87

Furlong, K.P., and Schwartz, S.Y. (2004). Influence of the Mendocino triple junction on the tectonics of coastal California. *Annual Review of Earth and Planetary Sciences,* 32, 403-433.

Goldstein, R.M., Engelhardt, H., Kamb, B., Frolich, R.M. (1993). Satellite radar interferometry for monitoring ice sheet motion; application to an Antarctic ice stream. *Science*, 262, 1525-1530.

Harvey, A.M. (2001). Coupling between hillslopes and channels in upland fluvial systems: implications for landscape sensitivity, illustrated from the Howgill Fells, northwest England. *Catena*, 42, 225–250.

Hilley, G. E., Bürgmann, R., Ferretti, A., et al. (2004). Dynamics of slow-moving landslides from permanent scatterer analysis. *Science*, 304, 1952-1955.

Hovius, N. Stark, C.P., and Allen, P.A. (1997). Sediment flux from a mountain belt derived by landslide mapping. *Geology (Boulder)*, 25, 231-234.

Hovius, N., Stark, C.P., Chu, H., et al. (2000). Supply and removal of sediment in a landslide-dominated mountain belt; Central Range, Taiwan. *Geology*, 108, 73-89.

Iverson, R. M. and Major, J.J. (1986). Rainfall, ground-water flow, and seasonal movement at Minor Creek landslide, northwestern California: Physical interpretation of empirical relations. *Geological Society of America Bulletin*, 99, 579-594.

Iverson, R.M. (2000). Landslide triggering by rain infiltration. *Water Resources Research*, 36, 1897-1910.

Keefer, D.K., and Johnson, A.M. (1983). Earth flows–Morphology, mobilization and movement. *U.S. Geological Survey Professional Paper*, 1264.

Kelsey, H. M. (1978). Earthflows in Franciscan melange, Van Duzen River basin, California. *Geology*, 6, 361-364.

Kimura, H. and Yamaguchi, Y. (2000). Detection of landslide areas using satellite radar interferometry. *Photogrammetric Engineering and Remote Sensing,* 66, 337– 344.

Mackey, B.H., Roering, J.J., and McKean, J.A. (2009). Long-term kinetics and sediment flux of an active earthflow, Eel River, California. *Geology*, 37, 803-806.

Massonnet D, Rossi M, Carmona C, Adragna F, Peltzer G, et al. (1993). The displacement field of the Landers earthquake mapped by radar interferometry. *Nature*, 364, 138–142.

Massonnet D, Briole P, Arnaud A. (1995). Deflation of Mount Etna monitored by spaceborne radar interferometry. *Nature,* 375, 567–570.

Massonnet, D., Feigl, K.L. (1998). Radar interferometry and its application to changes in the Earth's surface. *Reviews of Geophysics*, 36, 441–500.

Nolan, K.M. and Kelsey, H.M. (1995). Movement and sediment yield of two earthflows, northwestern California. *U.S. Geological Survey Professional Paper,* 1454.

Rosen, P.A., et al. (2004). Updated Repeat Orbit Interferometry Package Release, *Eos, Trans. AGU*, 85, 47.

Rott, H., Scheuchl, B., Siegel, A., Grasemann, B. (1999). Monitoring very slow slope movements by means of SAR interferometry: a case study from a mass waste above a reservoir in the Ötztal Alps, Austria. *Geophysical Research Letters*, 26, 1629– 1632.

Squarzoni, C., Delacourt, C., and Allemand, P. (2003). Nine years of spatial and temporal evolution of the La Valette landslide observed by SAR interferometry. *Engineering Geology*, 68(1-2), 53-66.

Vietmeier, J., Wagner, W., and Dikau, R. (1999). Monitoring Moderate Slope Movements (Landslides) In The Southern French Alps Using Differential SAR Interferometry. Procedings of FRINGE'99, Web site: http://esrin.esa.it/-fringe99

Zebker, H.A., and Rosen, P. (1994). On the derivation of coseismic displacement fields using differential radar interferometry; the Landers earthquake. *International Geoscience and Remote Sensing Symposium*, 1, 286-288.